SCIENCE CHINA
Physics, Mechanics & Astronomy

•Article•

February 2022 Vol. 65 No. 2: 227511
https://doi.org/10.1007/s11433-021-1794-4

Observation of magnetic droplets in magnetic tunnel junctions

Kewen Shi[1†], Wenlong Cai[1†], Sheng Jiang[3,4,5†], Daoqian Zhu[1], Kaihua Cao[1,2], Zongxia Guo[1], Jiaqi Wei[1], Ao Du[1], Zhi Li[1,2], Yan Huang[1], Jialiang Yin[1,2], Johan Åkerman[3,4*], and Weisheng Zhao[1,2*]

[1] *Fert Beijing Institute, MIIT Key Laboratory of Spintronics, School of Integrated Circuit Science and Engineering, Beihang University, Beijing 100191, China;*
[2] *Beihang-Goertek Joint Microelectronics Institute, Qingdao Research Institute, Beihang University, Qingdao 266000, China;*
[3] *Department of Physics, University of Gothenburg, Gothenburg 41296, Sweden;*
[4] *Department of Applied Physics, School of Engineering Sciences, KTH Royal Institute of Technology, Kista 16440, Sweden;*
[5] *School of Microelectronics, Northwestern Polytechnical University, Xi'an 710072, China*

Received July 12, 2021; accepted October 9, 2021; published online December 30, 2021

Magnetic droplets, a class of highly nonlinear magnetodynamic solitons, can be nucleated and stabilized in nanocontact spin-torque nano-oscillators. Here we experimentally demonstrate magnetic droplets in magnetic tunnel junctions (MTJs). The droplet nucleation is accompanied by power enhancement compared with its ferromagnetic resonance modes. The nucleation and stabilization of droplets are ascribed to the double-CoFeB free-layer structure in the all-perpendicular MTJ, which provides a low Zhang-Li torque and a high pinning field. Our results enable better electrical sensitivity in fundamental studies of droplets and show that the droplets can be utilized in MTJ-based applications and materials science.

spin-torque nano-oscillators, magnetic droplets, spin dynamics, magnetic tunnel junctions

PACS number(s): 75.78.-n, 75.30.Ds, 85.75.Dd

Citation: K. Shi, W. Cai, S. Jiang, D. Zhu, K. Cao, Z. Guo, J. Wei, A. Du, Z. Li, Y. Huang, J. Yin, J. Åkerman, and W. Zhao, Observation of magnetic droplets in magnetic tunnel junctions, Sci. China-Phys. Mech. Astron. **65**, 227511 (2022), https://doi.org/10.1007/s11433-021-1794-4

1 Introduction

Magnetic tunnel junction (MTJ)-based spin-torque nano-oscillators (STNOs) have recently attracted wide interest in nanomagnetism and spintronics [1-4]. As broadband microwave signal generators, STNOs are able to generate signals with frequencies ranging from a few MHz up to a hundred GHz [5-8], leading to potential applications in radio frequency electronics and artificial intelligence [9-11]. Nevertheless, achieving high output power is still a challenge for conventional STNOs [7]. Magnetic and magnetodynamic structures [12-14], such as vortices [15], bullets [16,17], and droplets [18], may provide a way to increase power emission as they maximize the use of available magnetoresistance thanks to their high precession amplitude. In particular, magnetic droplets with a central region that exhibits nearly opposite magnetization to its equilibrium state, with a perimeter manifesting 90° precession, are observed in nanocontact STNOs with strong perpendicular magnetic anisotropy (PMA) [19,20]. The microwave output power of the magnetic droplet mode was reportedly 40 times higher than that of a normal ferromagnetic resonance (FMR)-like mode related to uniform precession induced by spin-transfer

*Corresponding authors (Johan Åkerman, email: johan.akerman@physics.gu.se; Weisheng Zhao, email: weisheng.zhao@buaa.edu.cn)
†These authors contributed equally to this work.

torque, whose precession frequency is close to the ferromagnetic resonance frequency. This was mainly due to the large precession angle of the magnetic droplet mode [7,18,19]. However, all experimental work on magnetic droplets has, until now, focused on spin-valve (SV) structures [18,19,21-23] and spin-hall nano-oscillators (SHNOs) [24,25]. The very low magnetoresistance (MR) (approximately 1%) in SVs and SHNOs limits power emission and any further use in STNO-based applications. Comparatively, magnetic tunneling junctions with strong PMA (pMTJs) have presented a high tunneling magnetoresistance (TMR), reaching 249%, especially for the double-CoFeB free layer (DFL) pMTJ, which has become the main structure in MTJ-based MRAM [26]. Therefore, one might expect to observe magnetic droplets in pMTJ-based NC-STNOs. Nevertheless, our previous experiment shows that it is difficult to form a stable droplet in a single-free layer (SFL) MTJ [27]. This may result from the large Zhang-Li torque generated from the interaction between a uniform electric current density and a spatially varying magnetization. In contrast, DFL pMTJs are expected to suppress this large Zhang-Li torque and benefit the formation of a stable magnetic droplet.

Here we experimentally observe and investigate stable magnetic droplets in a DFL pMTJ accompanied by power enhancement with respect to FMR-like mode precession in the same device. Furthermore, using micromagnetic simulations, we argue that the stable magnetic droplets in MTJs are mainly due to the combination of the low Zhang-Li torque and the strong pinning field in the DFL [28]. Our findings provide a comprehensive understanding of the nucleation of magnetic droplets in MTJs and will pave the way for further optimizing the use of magnetic droplets in MTJs.

2 Materials and method

2.1 Sample fabrication

The pMTJs were deposited on a thermally oxidized Si substrate (300 nm SiO_2) by a Singulus TIMARIS 200-mm magnetron sputtering machine. The full stacks were composed of thickness in nanometers, from the substrate side, Ta(3)/Ru(20)/Ta(0.7)/Pt(1.5)/[Co(0.5)/Pt(0.35)]6/Co(0.6)/Ru(0.8)/Co(0.6)/[Pt(0.35)/Co(0.5)]3/Pt(0.25)/Ta(0.2)/Co(1.2)/W(0.25)/CoFeB(0.9)/MgO(~0.8)/CoFeB(1.2)/W(0.3)/CoFeB(0.5)/MgO(~0.8)/Pt(1.5)/Ta(3)/Ru(7). The pMTJ films were annealed at 390°C for 1 h. The wafer was patterned into a 10 μm×10 μm structure using optical lithography and etched to the Ru(20) seed layer using ion beam etching, where the ground electrode was connected to the seed layer. Then, the pMTJs were fully covered by SiO_2 deposited by chemical vapor deposition. A nanocontact, 100 nm in size, was fabricated using electron beam lithography and inductively coupled plasma etch with an optical emission spectrometer. Finally, a Ti(20)/Pt(200) top electrode was fabricated using a lift-off process.

2.2 Device characterization

The magnetization of the film was carried out using a vibrating sample magnetometer (VSM) instrument. Direct current (dc) and microwave characterization of the NC-STNO devices were measured using a custom-built probe station that was capable of independently controlling the field magnitude and angle. The dc current was provided by a Keithley 6221 current source, and voltage was measured with a Keithley 2182 nanovoltmeter. The generated microwave signals were decoupled from the dc current via a bias tee, amplified by a low-noise amplifier of the bandwidth 0.1-25 GHz, and analyzed using a Rohde & Schwarz FSU spectrum analyzer.

2.3 Simulations

Micromagnetic simulations were performed on a graphics processing unit (GPU)-based tool, Mumax336. An NC-STNO geometry was modeled in our simulations. The diameter of an MTJ was 240 nm, while that of the nanocontact above the MTJ was 100 nm (Figure S1, Supporting information online). Though the size of the simulated device was much smaller than our sample, we consider it a reasonable simplification to capture the physical picture of our experiments because the current is roughly distributed within the nanocontact area, even when the simulated geometry was enlarged to 1 μm. The free layer was set as 1-nm for the SFL MTJ. In contrast, the DFL MTJ was represented by two ferromagnetically coupled magnetic layers, with thicknesses of 0.5 and 1 nm for the top and bottom layers, respectively. The spacer between the two layers was omitted. A discrete mesh of 2 nm × 2 nm × 0.5 nm was used in our simulations.

The magnetization dynamics of each site in the free layer were numerically calculated using the Landau-Lifshitz-Gilbert (LLG) equation with spin-transfer torque (STT) and Zhang-Li torque included (see Supplementary note S1). The following magnetic parameters were used: a spin polarization ratio P=0.4, exchange constant A=15 pJ m^{-1}, the saturation magnetization M_s=987 KA m^{-1} from VSM results, Gilbert damping α=0.0218, and anisotropy energy density K_u=0.66 × 106 J m^{-3} from FMR results. If no pinning effect is considered, the DMI strength, D, is set to zero, and the exchange stiffness between the coupled two free layers is set as 2.5×10^{-14} J m^{-1}, which corresponds to an interlayer coupling strength of 0.1 mJ m^{-2}. When introducing the pinning effect, we set D=±0.5 mJ m^{-2} for the two coupled layers. In the meantime, the spatial distribution of interlayer coupling strength, from 0.04 to 0.1 mJ m^{-2}, was set using a Voronoi tessellation with an average size of 5 nm. The current dis-

tribution in the free layer was simulated using COMSOL software (Figure S2) and employed as an input in the micromagnetic simulations.

3 Results and discussion

Figure 1(a) shows a schematic and stack information for our NC-STNO device. The film stack is composed of a [Co/Pt]-based pinned layer (PL), a CoFeB reference layer (RL), and a CoFeB/W/CoFeB coupled DFL, both with strong PMA. Figure 1(b) shows the out-of-plane (OOP) and in-plane (IP) magnetization hysteresis loops of a corresponding unpatterned film. The IP hysteresis loop shows a typical hard-axis response, while the OOP hysteresis loop exhibits three distinct switching fields, each corresponding to the switching of the RL, DFL, and PL. The M_s of the DFL is about 987 kA/m. The PMA field ($\mu_0 H_k$) is 120.9(8) mT (Figure S1). A TMR ratio of 12.6% was measured in the fully processed STNO (Figure 1(c)). The measured low TMR of nanocontact devices mainly comes from the two-probe measurement method. Meanwhile, the current shunt of the nanocontact and Ta-pillar hard mask further decrease the obtained TMR ratio.

After confirming the static behavior, we study the magnetodynamics in Figure 2. At a moderate external magnetic field, sweeping from 100 to 25 mT with the direction θ_{ext}= 30°, a significant high-frequency signal is observed. This signal is shown in Figure 2(a) and corresponds to the ordinary FMR-like mode. When the field is swept back to lower than 20 mT, a new mode appears. The frequency abruptly drops to approximately 1 GHz (see details from PSD spectra in the inset of Figure 2(b)), and the microwave power increases from 2 to nearly 600 pW. Simultaneously, the resistance jumps to an intermediate state between antiparallel (AP) and parallel (P) states (pink line in Figure 2(a)). An approximately 1 GHz dynamic signal with an enhanced power emission accompanied by the intermediate resistance state is also observed in the angular-dependent measurements in Figure 2(c) and (d). Another significant feature of the droplet soliton is the low-*f* noise, as shown in Figure 2(a), which is caused by drift instability and subsequent renucleation [29]. We found that the low-*f* noise and weak dependence of field and current present an obvious peak at approximately 200 MHz, which is far from the 1/*f* noise caused by STT-induced incoherent precession [30,31]. All of these observations indicate that the observed new dynamic

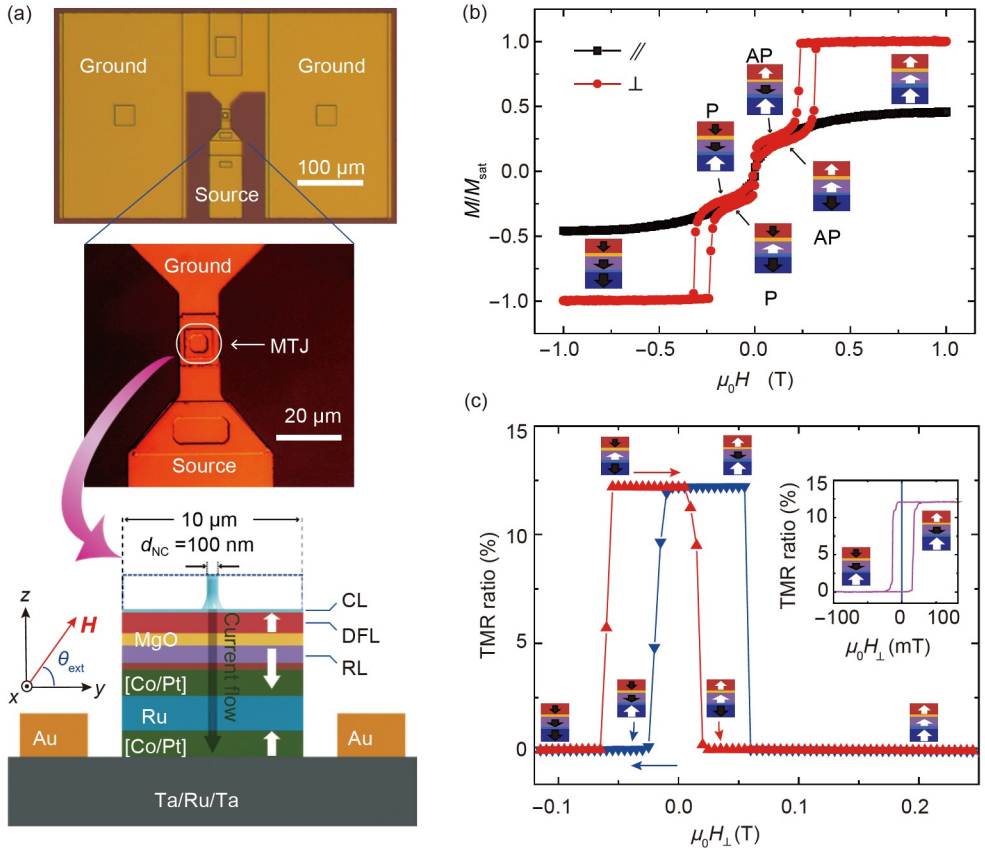

Figure 1 (Color online) (a) Schematic of the pMTJ STNO device. An external magnetic field, H, is applied at an angle θ_{ext}. (b) Magnetization hysteresis loops of the film normalized to the saturation magnetization, M_{sat}. (c) TMR loops measured at I=−0.1 mA. Positive current flows from the source to the ground.

structures are fully consistent with the nucleation of the magnetic droplet solitons.

Considering that the breath of skyrmions, the reference instabilities of MTJs, or domain wall dynamics may also generate an oscillation signal of a few GHz, we further discuss the possible alternative explanations. First, the structure symmetry of CoFeB/W/CoFeB results in a weak Dzyaloshinsky-Moriya interaction (DMI) [28], indicating that the skyrmion should be difficult to stabilize in our device at room temperature. Second, the reference-instability-induced oscillation only occurs during magnetization switching from P to AP states. As a comparison, signals of a few GHz are observed in both the P to AP and AP to P switching processes in this work. Due to the current shunt in our MTJ, the current density in the RL is approximately 1 MA cm^{-2}, which is not sufficient to induce RL instabilities. Third, the approximately 1 GHz signal, low-*f* noise, exists until −50 mT for −2.4 mA and 40 mT for 2.4 mA (Figure S4) with an angle of 60°, at which the magnetization of the free layer is supposed to be saturated. Figure 2(e) shows the perpendicular field-swept resistance measurements at different negative currents. As the dashed lines show, the saturated magnetic fields for DFL should be larger than 25 mT or less than −20 mT. However, it is obvious that the STT torques could form intermediate resistance states under saturated magnetic fields, which are always accompanied by the low-*f* noise shown in Figure 2(g). Due to the collinearity between FL and RL magnetizations under perpendicular fields, no high-frequency signals are expected [29]. Moreover, the intermediate resistance state boundaries (nucleation boundaries) show a linear dependence on both current and field in Figure 2(e), which is similar to the droplet boundary in SVs [21]. Since the saturated magnetic fields could suppress the domains rather than the droplets, we conclude that this observed dynamic structure is more likely a magnetic droplet. Future studies using scanning transmission X-ray microscopy at a synchrotron facility could potentially determine an intuitive image of the observed magnetic droplets.

Upon further characterization, we found another state that has an intermediate resistance but no low-*f* noise. To further clarify the nature of this apparently non-dynamical state, we measured frequency spectra under perpendicular field sweeps at I=−1.6 mA and current sweeps at a field of $\mu_0 H$= −15 mT, with an angle of θ_{ext}=30°, as shown in Figure 3(a) and (b), respectively. When the field is swept in the negative direction, the magnetization of the DFL stays AP to the RL's magnetization from 30 to 5 mT without STT, as shown in Figure 1(c). However, since the STT from the negative applied current favors the AP state, the magnetization instead tends to maintain the original AP state underneath the nanocontact area, while only the DFL area outside of the nanocontact switches to the P state. This partial switching of magnetization induces an intermediate resistance state, which is slightly higher than the resistance of the droplet and is completely void of any accompanying low-*f* noise. Hence, this novel partially reversed state is not a precessing droplet

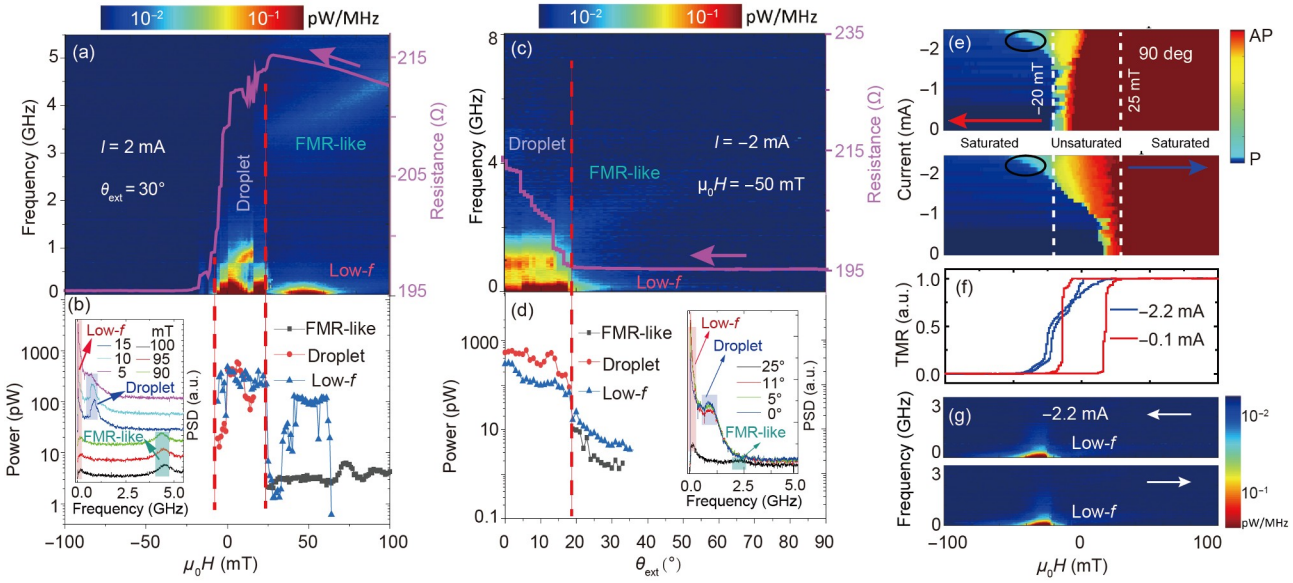

Figure 2 (Color online) Dynamical properties of magnetic droplets. Power spectral density (PSD) (left) and resistance (right) as functions of (a) magnetic field applied at an angle of 30° and I=2 mA, and (c) angle at $\mu_0 H$=20 mT and I=−1.6 mA. The pink solid lines give the resistance curves. The corresponding integrated powers as functions of (b) magnetic field and (d) angle. The red vertical dotted lines display the critical points in the dynamic and static properties. Insets in (b) and (d) show the PSD under different magnetic field values and different magnetic field angles, respectively. A frequency drop can be clearly observed during the transformation from FMR-like mode to droplet mode. (e) Perpendicular magnetic field-swept resistance measurements at different negative currents. The dashed white lines marked the unsaturated fields for DFL. (f) The corresponding magnetoresistance plots under −0.1 and −2.2 mA. (g) PSD as a function of the perpendicular magnetic field with I=−2.2 mA. The low-*f* noises are accompanied by the intermediated resistance states marked by the circles in (e).

but more likely a "static magnetic bubble" with a reversed core. This is similar to SV-based NC-STNOs [32,33], where the current density is not sufficient to maintain the droplet in a state of precession. The bubble state remains stable until the external magnetic field is swept down to −14 mT. By increasing the fields, the pressure on the static bubble makes it shrink until it again transforms into a precessing droplet with a step-like decrease of resistance and the reappearance of low-*f* noise. The transformation from a static bubble to a precessing droplet may result from the STT becoming strong enough to again compensate for the damping torque as the magnetic field pushes the bubble perimeter into the nano-contact region. The field sweeping from negative to positive shows a similar property.

As for the current sweep in Figure 3(b), the P state switches into a droplet state with a low-*f* noise and the step-like increase of the resistance at a threshold current of I_{th}= −1.57 mA. The approximately 1 GHz signals that the magnetic droplet could also be observed during the current sweep, as shown in Figure 3(b). The magnetic droplet is stable while the current is further decreased to −2.2 mA. When the current is swept back, the droplet still exists even though the current is much lower than the threshold current, I_{th}, of droplet nucleation. As the low-*f* noise damps out at around −0.9 mA, the dynamic droplet starts to slow down and turns into a static bubble at a lower current with the disappearance of the approximately 1 GHz signal. The obvious hysteresis indicates the different magnitude of stimulus that is required for droplet nucleation and annihilation [19].

We note that the threshold current density of droplet nucleation in our devices can be as low as approximately 5 MA cm^{-2} with a magnetic field of approximately 20 mT, which is quite less than that in the SVs (approximately 130 MA cm^{-2} under 0.25 T) [21]. Such low current density could be associated with (1) slightly lower damping (0.02 for CoFeB here, 0.03 for [Co/Ni] multilayers [21]), (2) different spin-torque efficiency, and (3) different device structures inducing different current distributions, and so on. We would also like to emphasize here that the lower threshold current density for droplets is critical in MTJs with a power emission of up to 600 pW, providing an approximately 300 times enhancement (compared with the FMR-like mode signal), which is more advantageous than that in SVs or SHNOs (Table S1, Supporting information online).

In contrast to our previous work on an SFL MTJ [27], magnetic droplets are successfully observed in a DFL MTJ here. To clarify the essential difference, we performed micromagnetic simulations to further analyze the stability of the magnetic droplets. Usually, the size of the droplet is determined by a combination of factors, such as the external magnetic field, the Zhang-Li torque induced by realistic lateral current spreading [21], and the pinning field of the free layer. For comparison, we calculated the current distribution in free layers of an SFL MTJ and an SV using COMSOL. The lateral current spread, $-J_x$, is much higher in MTJs than that in SVs [21] due to the existence of the MgO barrier. Such high $-J_x$ induces a larger Zhang-Li torque in the free layer. Consequently, it further hinders the observation of stable droplets in MTJs. To explain the reason for stable droplets in our DFL MTJ, we conducted the same current distribution calculation and a micromagnetic simulation as shown in Figure 4. In contrast, the $-J_x$ in DFL (usually with a MgO capping layer (CL) [26]) is near half of that in the SFL MTJs. It is associated with current shunting at the MgO in the CL before entering the free layer, although this may consume a bit more current in the CL. For this reason, it

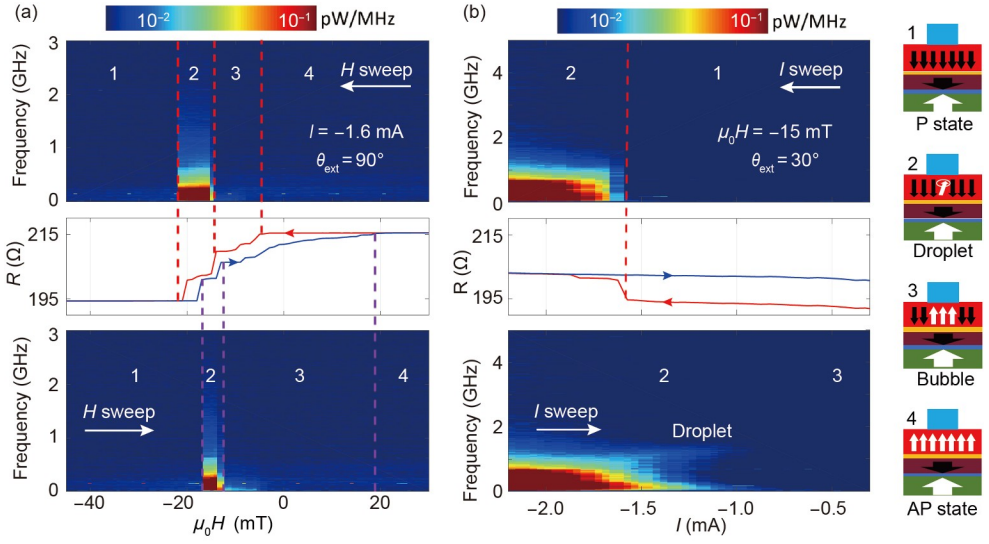

Figure 3 (Color online) Frequency spectra and resistance as functions of (a) external perpendicular magnetic field (I=−1.6 mA) and (b) current ($\mu_0 H$=−15 mT, θ_{ext}=30°). The models on the right represent possible magnetic states: P state, Droplet, Bubble, and AP state, named 1, 2, 3, and 4, respectively, and corresponding to the MR and PSD results for the NC-STNO.

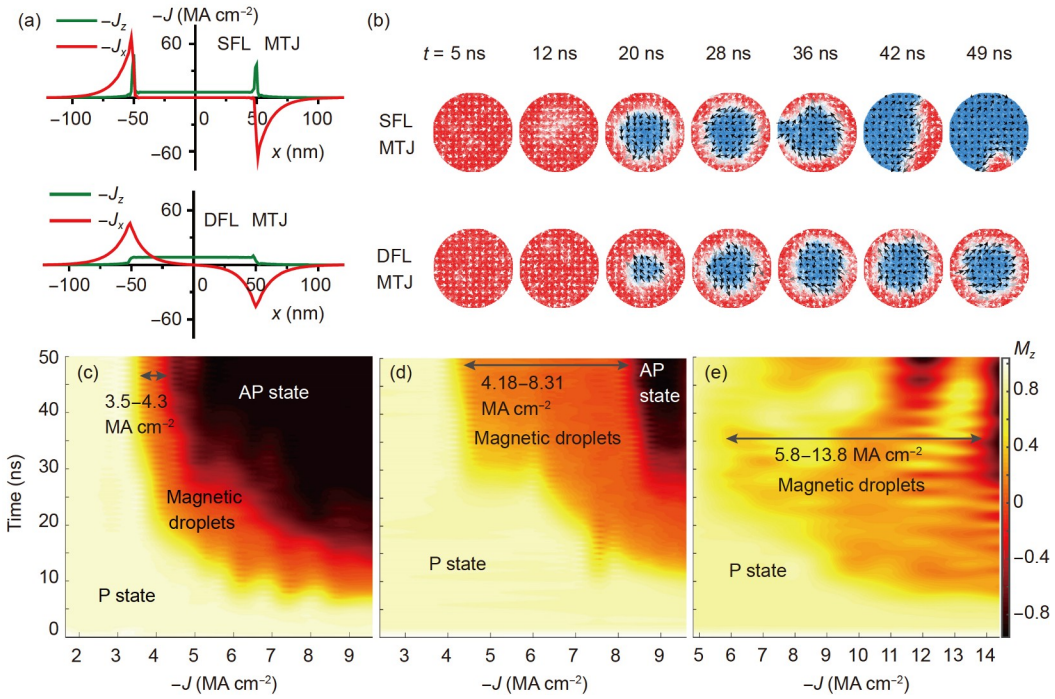

Figure 4 (Color online) (a) Distributions of current in the free layers of SFL and DFL MTJs. (b) Comparison of magnetization evolution under selected time between SFL and DFL where the current density is −7 MA cm^{-2}. (c)-(e) Plots of current magnitude vs. time for the nucleation of magnetic droplets in SFL MTJ, DFL MTJ, and DFL MTJ with RKKY and DMI distribution. The horizontal arrows present the current range for stable magnetic droplets. All simulations were performed at −10 mT and 300 K. The initial state for the device is the P state.

should be easier to obtain and stabilize the magnetic droplets in a DFL than in an SFL. Figure 4(b) shows the magnetization evolution of SFL and DFL MTJs. The magnetization at the edge of the dynamics is mostly in the same direction, indicating that this structure should be a droplet rather than a skyrmion. Moreover, the evolution of droplet nucleation or annihilation in SFL and DFL MTJs is displayed in Figure 4(c) and (d). The region for a stable magnetic droplet is apparently wider in the DFL ($-J$=4.18-8.31 MA cm^{-2}) than that in an SFL ($-J$=3.5-4.3 MA cm^{-2}).

Moreover, an inhomogeneous and thin W insert layer between double-free layers can cause local DMI and nonuniform RKKY distribution, which induces a much higher pinning field [28] compared with SFL MTJs. To determine the influence of this pinning field, we performed a simulation for a DFL MTJ with the RKKY distribution and DMI in Figure 4(e). The range for nucleation of magnetic droplets becomes wider, indicating that the higher pinning field in our DFL MTJ highly stabilizes the observed magnetic droplets.

4 Conclusions

A magnetic droplet is experimentally observed in a nanocontact pMTJ-STNO with DFL structures. Due to the introduction of the DFL, the low Zhang-Li torque and high pinning field have been identified to be responsible for the stabilization of the magnetic droplet. The relatively high TMR of MTJs, compared with the low MR of SVs, enables one order of magnitude smaller current density to induce a comparative power emission. Furthermore, experimental results reveal the transformation from a static magnetic bubble to a precessional droplet by tuning the magnetic field and the STT. Droplet implementation in MTJs provides a comprehensive understanding of nucleation and stabilization of magnetic droplets in MTJs and launches an alternative path toward exploring applications of spintronic devices.

This work was supported by the Beijing Municipal Science and Technology Project (Grant No. Z201100004220002), the National Natural Science Foundation of China (Grant Nos. 61627813, and 61904009), and the China Postdoctoral Science Foundation Funded Project (Grant No. 2018M641151).

Supporting Information

The supporting information is available online at phys.scichina.com and http://link.springer.com/journal/11433. The supporting materials are published as submitted, without typesetting or editing. The responsibility for scientific accuracy and content remains entirely with the authors.

1 A. Houshang, R. Khymyn, H. Fulara, A. Gangwar, M. Haidar, S. R. Etesami, R. Ferreira, P. P. Freitas, M. Dvornik, R. K. Dumas, and J. Åkerman, Nat. Commun. **9**, 4374 (2018), arXiv: 1712.00954.
2 B. Fang, M. Carpentieri, X. Hao, H. Jiang, J. A. Katine, I. N. Krivorotov, B. Ocker, J. Langer, K. L. Wang, B. Zhang, B. Azzerboni, P. K. Amiri, G. Finocchio, and Z. Zeng, Nat. Commun. **7**, 11259 (2016).
3 A. V. Chumak, V. I. Vasyuchka, A. A. Serga, and B. Hillebrands, Nat. Phys. **11**, 453 (2015).
4 A. Litvinenko, V. Iurchuk, P. Sethi, S. Louis, V. Tyberkevych, J. Li, A. Jenkins, R. Ferreira, B. Dieny, A. Slavin, and U. Ebels, Nano Lett. **20**, 6104 (2020), arXiv: 2004.03508.
5 S. Bonetti, P. Muduli, F. Mancoff, and J. Åkerman, Appl. Phys. Lett. **94**, 102507 (2009).
6 I. Lisenkov, R. Khymyn, J. Åkerman, N. X. Sun, and B. A. Ivanov, Phys. Rev. B **100**, 100409 (2019), arXiv: 1904.09341.
7 T. Chen, R. K. Dumas, A. Eklund, P. K. Muduli, A. Houshang, A. A. Awad, P. Durrenfeld, B. G. Malm, A. Rusu, and J. Akerman, Proc. IEEE **104**, 1919 (2016).
8 Z. Zeng, G. Finocchio, and H. Jiang, Nanoscale **5**, 2219 (2013), arXiv: 1302.6467.
9 M. Zahedinejad, A. A. Awad, S. Muralidhar, R. Khymyn, H. Fulara, H. Mazraati, M. Dvornik, and J. Åkerman, Nat. Nanotechnol. **15**, 47 (2020).
10 Y. J. Zhang, Q. Zheng, X. R. Zhu, Z. Yuan, and K. Xia, Sci. China-Phys. Mech. Astron. **63**, 277531 (2020).
11 W. Fon, M. H. Matheny, J. Li, L. Krayzman, M. C. Cross, R. M. D'Souza, J. P. Crutchfield, and M. L. Roukes, Nano Lett. **17**, 5977 (2017).
12 A. M. Kosevich, B. A. Ivanov, and A. S. Kovalev, Phys. Rep. **194**, 117 (1990).
13 H. B. Braun, Adv. Phys. **61**, 1 (2012).
14 O. R. Sulymenko, O. V. Prokopenko, V. S. Tyberkevych, A. N. Slavin, and A. A. Serga, Low Temperature Phys. **44**, 602 (2018).
15 V. S. Pribiag, I. N. Krivorotov, G. D. Fuchs, P. M. Braganca, O. Ozatay, J. C. Sankey, D. C. Ralph, and R. A. Buhrman, Nat. Phys. **3**, 498 (2007), arXiv: cond-mat/0702253.
16 R. K. Dumas, E. Iacocca, S. Bonetti, S. R. Sani, S. M. Mohseni, A. Eklund, J. Persson, O. Heinonen, and J. Åkerman, Phys. Rev. Lett. **110**, 257202 (2013), arXiv: 1303.7148.
17 S. Bonetti, V. Tiberkevich, G. Consolo, G. Finocchio, P. Muduli, F. Mancoff, A. Slavin, and J. Akerman, Phys. Rev. Lett. **105**, 217204 (2010), arXiv: 0909.3331.
18 S. M. Mohseni, S. R. Sani, J. Persson, T. N. A. Nguyen, S. Chung, Y. Pogoryelov, P. K. Muduli, E. Iacocca, A. Eklund, R. K. Dumas, S. Bonetti, A. Deac, M. A. Hoefer, and J. Akerman, Science **339**, 1295 (2013).
19 F. Macià, D. Backes, and A. D. Kent, Nat. Nanotechnol. **9**, 992 (2014), arXiv: 1408.1902.
20 S. Chung, A. Eklund, E. Iacocca, S. M. Mohseni, S. R. Sani, L. Bookman, M. A. Hoefer, R. K. Dumas, and J. Åkerman, Nat. Commun. **7**, 11209 (2016).
21 S. Chung, Q. T. Le, M. Ahlberg, A. A. Awad, M. Weigand, I. Bykova, R. Khymyn, M. Dvornik, H. Mazraati, A. Houshang, S. Jiang, T. N. A. Nguyen, E. Goering, G. Schütz, J. Gräfe, and J. Åkerman, Phys. Rev. Lett. **120**, 217204 (2018).
22 N. Statuto, J. M. Hernàndez, A. D. Kent, and F. Macià, Nanotechnology **29**, 325302 (2018), arXiv: 1803.01750.
23 J. Hang, C. Hahn, N. Statuto, F. Macia, and A. D. Kent, Sci. Rep. **8**, 6847 (2018).
24 B. Divinskiy, S. Urazhdin, V. E. Demidov, A. Kozhanov, A. P. Nosov, A. B. Rinkevich, and S. O. Demokritov, Phys. Rev. B **96**, 224419 (2017), arXiv: 1710.04430.
25 L. Chen, S. Urazhdin, K. Zhou, Y. W. Du, and R. H. Liu, Phys. Rev. Appl. **13**, 024034 (2020).
26 M. Wang, W. Cai, K. Cao, J. Zhou, J. Wrona, S. Peng, H. Yang, J. Wei, W. Kang, Y. Zhang, J. Langer, B. Ocker, A. Fert, and W. Zhao, Nat. Commun. **9**, 671 (2018), arXiv: 1708.04111.
27 S. Jiang, M. Ahlberg, S. Chung, A. Houshang, R. Ferreira, P. P. Freitas, and J. Åkerman, Appl. Phys. Lett. **115**, 152402 (2019), arXiv: 1907.10427.
28 X. Zhang, W. Cai, M. Wang, B. Pan, K. Cao, M. Guo, T. Zhang, H. Cheng, S. Li, D. Zhu, L. Wang, F. Shi, J. Du, and W. Zhao, Adv. Sci. **8**, 2004645 (2021).
29 S. Lendínez, N. Statuto, D. Backes, A. D. Kent, and F. Macià, Phys. Rev. B **92**, 174426 (2015), arXiv: 1507.08218.
30 A. M. Deac, A. Fukushima, H. Kubota, H. Maehara, Y. Suzuki, S. Yuasa, Y. Nagamine, K. Tsunekawa, D. D. Djayaprawira, and N. Watanabe, Nat. Phys. **4**, 803 (2008), arXiv: 0803.2013.
31 K. J. Lee, A. Deac, O. Redon, J. P. Nozières, and B. Dieny, Nat. Mater. **3**, 877 (2004), arXiv: cond-mat/0406628.
32 S. Jiang, *Engineering Magnetic Droplets in Nanocontact Spin-Torque Nano-Oscillators*, Dissertation for the Doctoral Degree (KTH Royal Institute of Technology, Stockholm, 2018).
33 A. Vansteenkiste, J. Leliaert, M. Dvornik, M. Helsen, F. Garcia-Sanchez, and B. Van Waeyenberge, AIP Adv. **4**, 107133 (2014), arXiv: 1406.7635.